Supplementary Information

Schematic structure of the developed membrane module

Fig. S1 shows an exploded view of the developed membrane module allowing continuous single pass diafiltration. The module consists of three 3D-printed parts (one middle part and two lateral parts) enclosing two commercial UF membranes. The lateral parts hold the flow channels for either diafiltration (DF) buffer or permeate, and the middle part provides the flow channel for feed respectively retentate. In order to increase the flow path length in a compact design, the flows are guided by U-shaped channels. All flow channels are filled by a grid structure providing a mechanical support for the membranes from both sides.

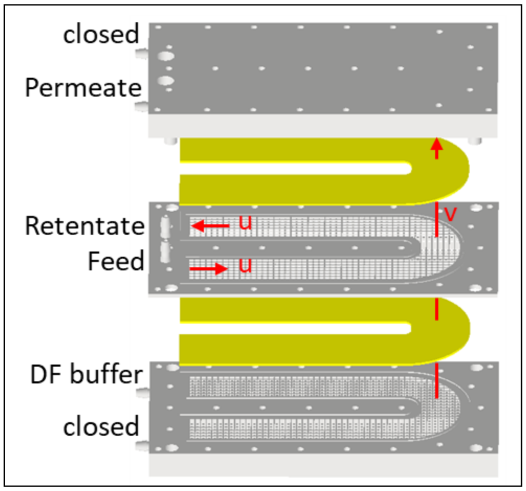

Fig. S1. Exploded view of the developed membrane module. The grid structures in the middle and lateral parts provide flow channels and at the same time mechanical support for the membranes.

Piping and instrumentation diagram of the experimental setup

Fig. S2 shows the piping and instrumentation diagram of the experimental setup used to test the developed diafiltration module. With the double piston pumps A, B, and C, the flow rates in the system can be adjusted precisely, independently of the occurring pressures. Switching of the flow direction of DF buffer is achieved by two computer controlled multi-port valves. The system includes two pressure sensors for online monitoring of the pressures in the retentate outlet as well as the DF buffer inlet. In addition, the system allows recording of the UV-signal at 280 nm and the conductivity of the retentate.

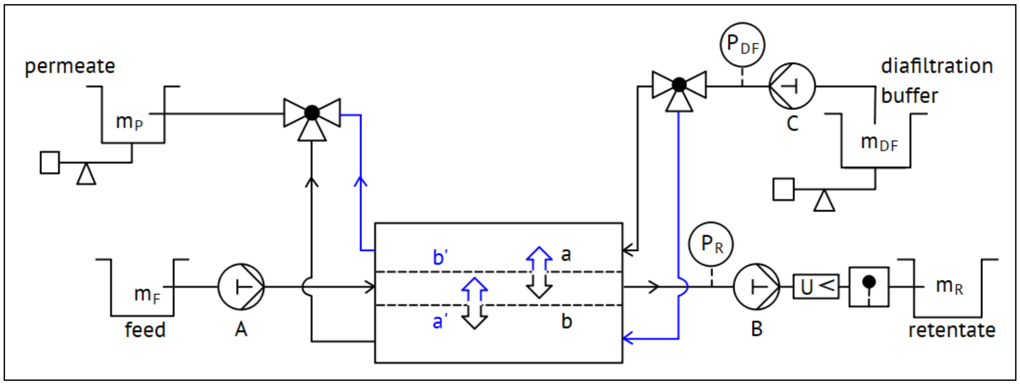

Fig. S2. Piping and instrumentation diagram of the experimental setup. The direction of the flows perfusing membrane a and b could be switched by means of the multiport valves of the FPLC system. The BSA and salt concentration in the retentate were monitored in real-time by UV and conductivity sensors, respectively. Adapted from Ref. [17].

Applied FEM mesh and simulated flow pattern in the module

For the simulations a quadratic mesh with inhomogeneous meshing is used. In order to reproduce the steep concentration profiles resulting during concentration polarization a very fine mesh is used in the vicinity of the membranes (see Fig. S3B). Fig. S3A shows a typical flow pattern of the simulated runs. The flow in the middle part is constant along the module length and, due to the pressure drop caused by the grid, shows only small variations in the y-direction. The flow rate in the upper lateral part decreases from its initial value in the DF buffer inlet down to zero at the left outlet, which is closed by a valve during this period. Along the module, the DF-buffer gradually permeates through the membrane into the middle part. The same amount of fluid leaves the middle part and leads to a gradual increase of the flow rate in the lower module part along the length of the module. The simulated flow patterns also clearly show that the flow velocity in the two artificial outlets is practically zero and that the flow pattern in the lateral parts is not influenced when flowing by.

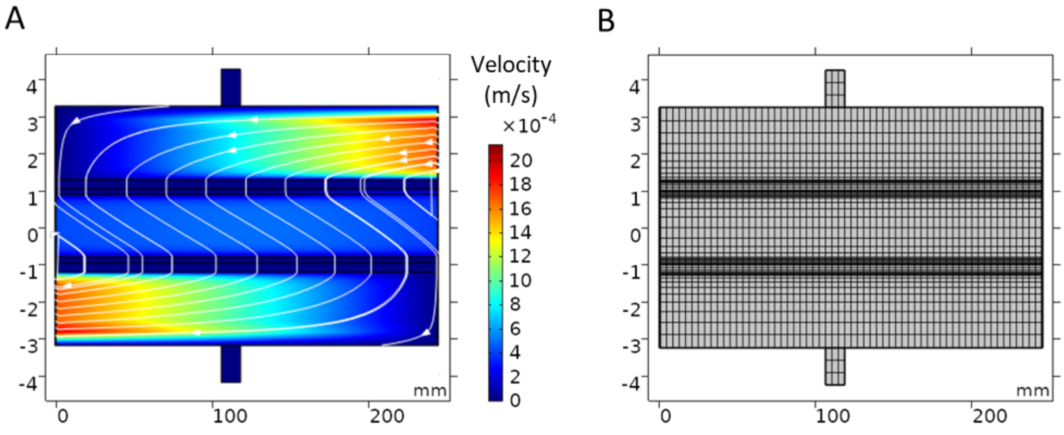

Fig. S3. Flow distribution within the membrane module and the applied mesh of the FEM calculations. A. Velocity field and flow path contours when applying the DF buffer from top to bottom; B. Generated quadratic mesh with increased mesh density in the vicinity of the membranes.

Detailed view of the 3D-printed grid structure within the flow channels of the module

The flow channels are filled by a hollow-carved grid with quadratic combs. The combs allow a free fluid flow in y-direction while the flow in x-direction is diverted and splitted by staggered holes in the grid walls.

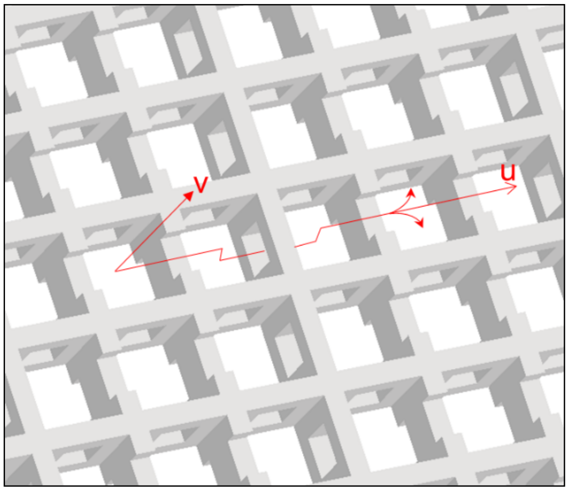

Fig. S4. Close-up of the grid structure supporting the membranes in the module from both sides. The flow in y-direction is without any obstacles while the flow in x-direction results in strong eddy diffusion effects.

Typical time course of the salt concentration in the retentate effluent

The concentration of salt detected in the retentate shows a wave-like fluctuation caused by the periodic switching of the flow direction of DF buffer. In the shown example the flow direction of DF buffer was switched every 180 s at a feed flow rate of 0.25 ml/min and 7.2 diavolumes. The simulated concentration of salt in the retentate varies from about 3.5 to 5.8 mol/m³. The average concentration is about 5 mol/m³, corresponding with a diafiltration efficiency of 95%.

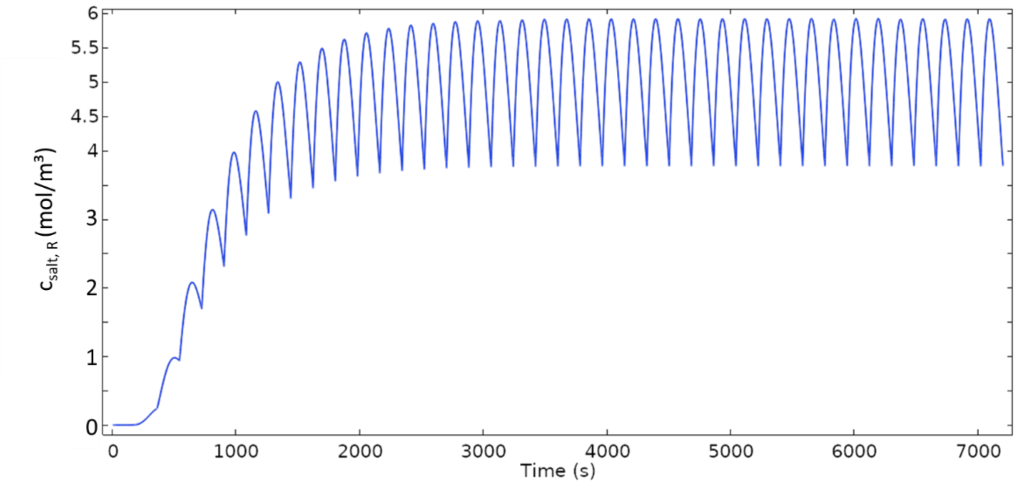

Fig. S5. Periodic fluctuations of the concentration of salt in the retentate for a simulated experiment with: $c_{F,salt}$ = 100 mM, Q_{DF} = 1.8 ml/min, Q_F = 0.25 ml/min and t_S = 180 s.

Representative BSA concentration contours in the quasi-stationary status

After simulation times of about three times the fluid residence time in the middle channel, the BSA concentration in the retentate is close to the one in the feed solution because the same feed and retentate flow rates are applied. At this quasi-stationary state, the freshly accumulated BSA amount in the boundary layer at the membrane surface equals the BSA amount leaving the module in the retentate. Shortly after switching the DF buffer flow direction, BSA moves to the opposite membrane in form of a concentrated fluid compartment stretching across the whole module.

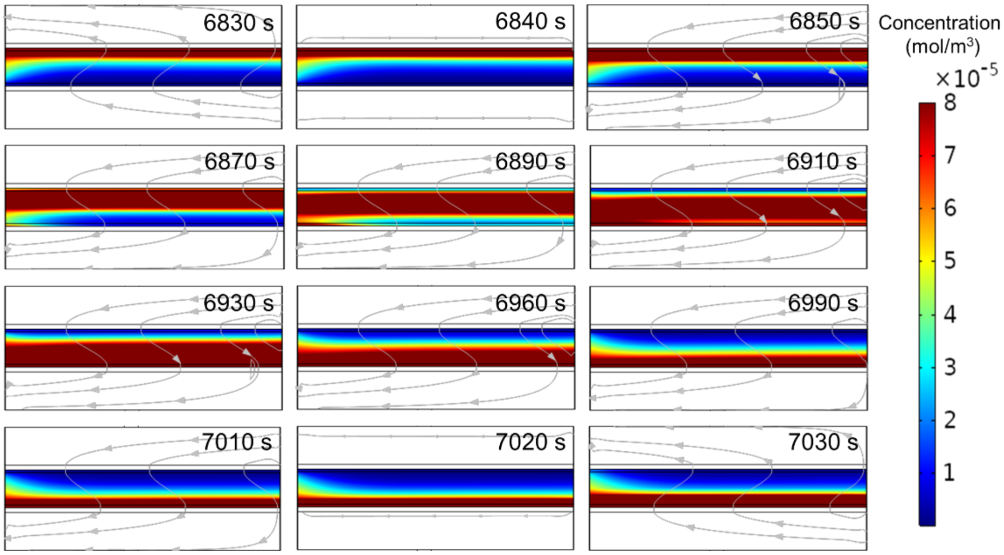

Fig. S6. Representative BSA distribution in the middle channel of the module at quasi-stationary state. The module was operated at a switching interval of 180 s.

Representative BSA concentration profiles in y-direction at different membrane positions

The BSA concentration profiles in y-direction at different membrane positions (x = 5, 122.5, 240 mm) are plotted for a simulation with: $c_{F,BSA} = 5$ g/L, $Q_F = 0.25$ ml/min, $Q_{DF} = 1.8$ ml/min and $t_S = 420$ s. The selected times represent the initial phase of before and after the first switching event as well as a situation when quasi-stationary state is reached. Nevertheless, also at quasi-stationary state the dynamic profiles change shortly before and after a switching event.

In the initial phase, the concentration profile at the beginning and the end of the flow channel (positions 5 and 240 mm) show a clear difference, while in quasi-stationary state BSA stretches along the x-direction almost homogenously. However, in y-direction the BSA profiles clearly show the effect of concentration polarization, accumulation BSA up to concentrations of around 160 g/L at the membrane surface.

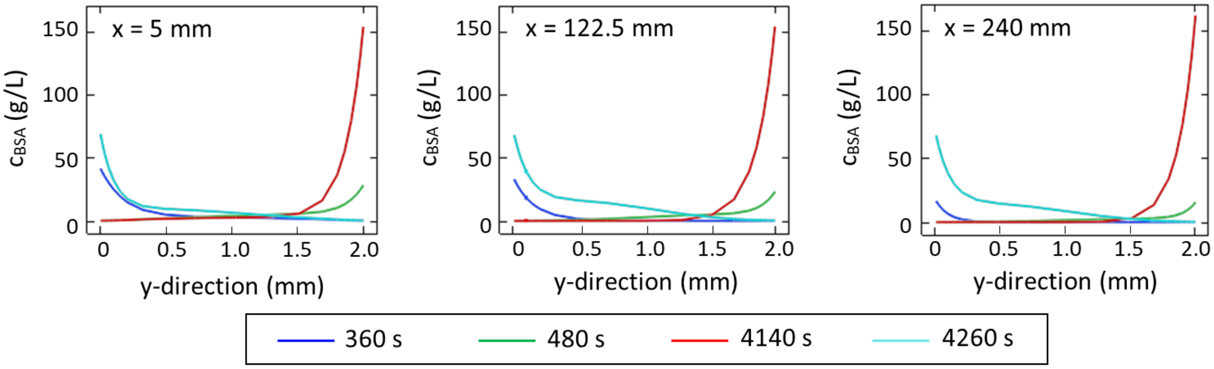

Fig. S7. Concentration profiles of BSA above the membrane at different position (x = 5, 122.5, 240 mm) and different times for a simulation with: $c_{F,BSA} = 5$ g/L, $Q_F = 0.25$ ml/min, $Q_{DF} = 1.8$ ml/min (7.2 diavolumes) and $t_S = 420$ s.

Time course of the pressure in the middle part of the module during a simulation with alternating flow direction of DF buffer

The pressure in the middle part increases during the period between two switching events. The pressure increase corresponds with the amount of accumulated BSA in the boundary layer above the membrane surface. When switching the flow direction of DF buffer, the pressure built-up drops abruptly and restarts the period of pressure increase at the intrinsic pressure drop of the membrane at the given flux.

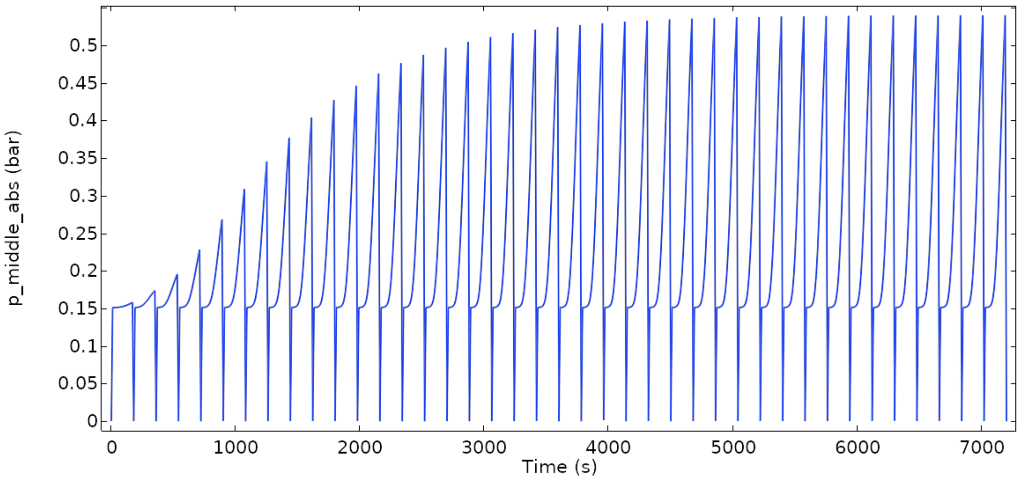

Fig. S8. Progression of the pressure in the middle part of the module for a simulation applying an alternating flow direction DF buffer. It was decided by the amount of the concentrated BSA at the membrane surface and the membrane area covered by the BSA, which is related to the hydrodynamic flow patterns.

Time course of the pressure in the upper module part for unidirectional DF buffer flow

In case of unidirectional DF buffer flow, the pressure in the upper module part reaches a plateau value in the course of a long-term simulation run without switching events. All simulations shown are conducted at DV = 5, $c_{F,BSA} = 5$ g/L, but varying feed flow rates Q_F. At higher Q_F the adjustment of the maximum pressure is achieved in a shorter time. For tangential flow filtration one may expect a reduced concentration polarization and consequently a reduced pressure built-up for higher Q_F values. However, in case of a constant number of diavolumes applied, the effect of the proportional increase of the required DF buffer flux prevails.

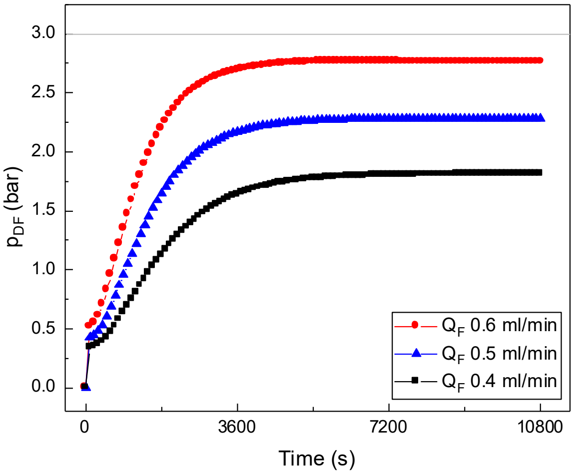

Fig. S9. Progression of pressure built-up in the DF buffer part with constant DV 5 at various flow rate of feed solution using unidirectional diafiltration.

Typical time course of the BSA concentration in the retentate when operating with switching DF buffer flow direction

The simulated BSA concentration in the retentate shows a wave-like fluctuation comparable to the one of salt shown in Fig. S4. However, a closer look reveals that due to BSA accumulation in the boundary layer, the adjustment of a quasi-stationary state requires longer times. In addition, the accumulated BSA causes stronger concentration fluctuations when the detached volume compartment including high BSA concentrations moves to the opposite membrane after a switching event.

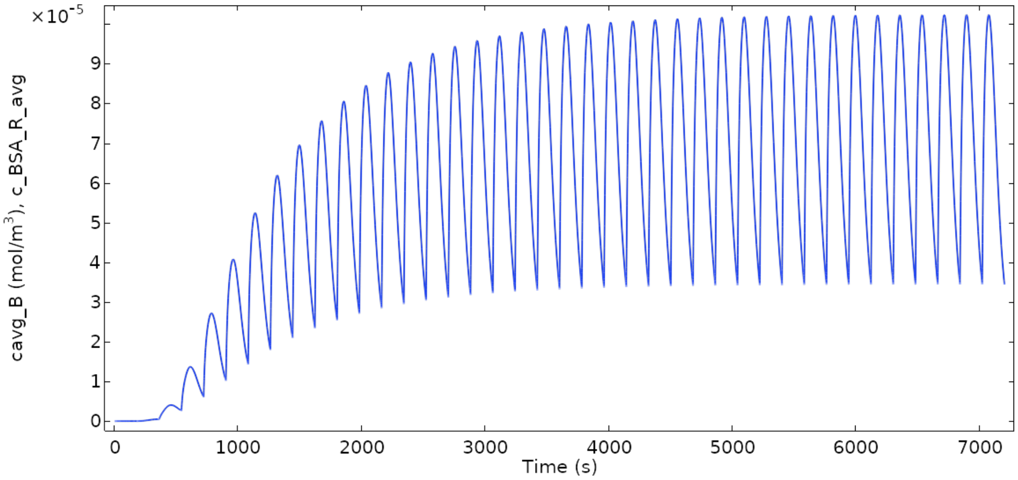

Fig. S10. Periodic fluctuations of the concentration of BSA in the retentate for a simulated experiment with: $c_{F,BSA} = 7.5 \cdot 10^{-5}$ mol/m^3 (5 g/L), $c_{F,salt} = 100$ mM, $Q_{DF} = 1.8$ ml/min, $Q_F = 0.25$ ml/min and $t_S = 180$ s.

Semi-empirical correlation describing the maximum pressure drop in the boundary layer (p_{BSA})

The results of the maximum pressure drop p_{BSA} in the boundary layer is plotted in Fig. S10 for 23 experiments ranging in their operation conditions from $c_{F,BSA} = 0$ - 5 g/L, DV = 7.2; 14.4, $t_s = 120$ - 420 s. In addition, the determined semi-empirical correlation is plotted. For the correlation we defined the effective mass flow rate of BSA, $\dot{N}_{BSA,eff}$, as the time weighted amount of BSA transported towards the membrane surface.

$$\dot{N}_{BSA,eff} = \; c_{F,\,BSA} \cdot Q_{DF} \cdot \frac{(Q_F \cdot t_S)^3}{2+\,(Q_F \cdot t_S)^3} \tag{S1}$$

In this term, the first part ($c_{F,\,BSA} \cdot Q_{DF}$) determines the maximum value of $\dot{N}_{BSA,eff}$ and therefore also the maximum pressure drop p_{BSA} in case of unidirectional flow of the DF buffer ($t_S \rightarrow \infty$). The second term describes how much this maximum pressure drop is reduced if a switching interval of t_s is applied. Besides, the switching interval the second term depends on the feed flow rate Q_F which itself is inversely proportional to the liquid residence time in the middle part of the module. As can be seen in Fig. S7, the defined effective mass flow rate shows a very good correlation to p_{BSA} with a calculated R^2 of 0.977. Based on this correlation, the theoretical p_{BSA} is predictable for any assigned combination of operation parameters in the mentioned range. This means vice versa, starting with a given pressure drop p_{BSA} and fixing the operation parameters except for one, the value of the unknown parameter can be estimated.

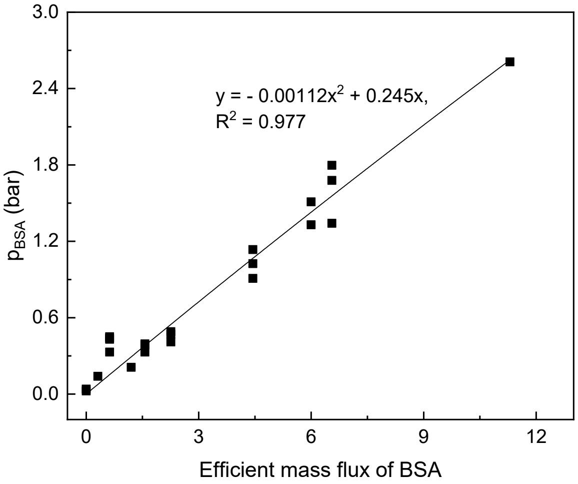

Fig. S11. Semi-empirical correlation between pressure between pressure drop in the boundary layer (p_{BSA}) and the effective mass flow rate of BSA.

Comparison of experimental and simulated results of pressure and diafiltration efficiency with high feed concentration of BSA

The experimental and simulated results of the maximum pressures in the module and the diafiltration efficiencies reached are shown in Fig. S12 for two cases of high feed concentrations of BSA at 20 and 50 g/L, respectively. Compared to the simulated pressures the experimental ones are about 0.3 bar higher, however, all pressures are much lower than the pressure limitation of the system (3 bar). For the diafiltration performance, experimental and simulated results are in excellent agreement.

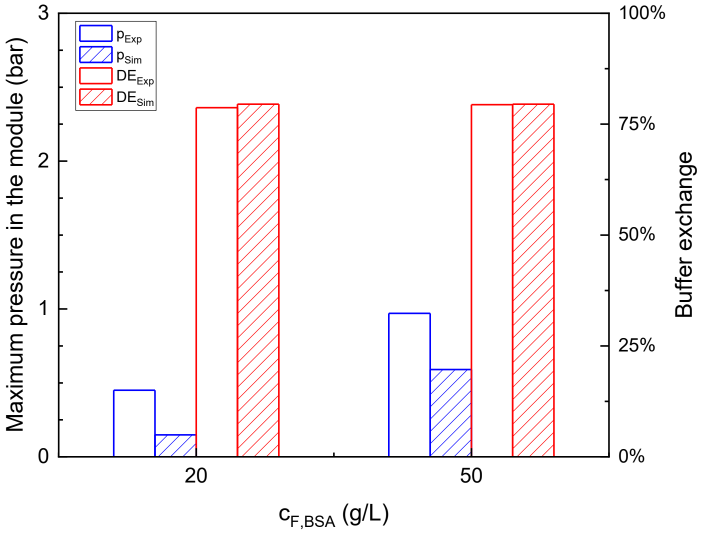

Fig. S12. Comparison of experimental and simulated results of the maximum pressures in the module and the diafiltration efficiencies reached in stationary operation. Experimental conditions: Feed concentration of BSA at 20 and 50 g/L, $Q_F = 0.2$ ml/min, $Q_{DF} = 0.4$ ml/min, unidirectional DF buffer flow.

S13. Derivation of equation 3 of the main text

The following section shows the mathematical derivation of eq. 3 of the main text:

$$\nabla \boldsymbol{p} = -\frac{\mu}{\kappa}\boldsymbol{u} + \frac{\mu}{\varepsilon}\nabla^2\boldsymbol{u} - \frac{\rho}{\varepsilon}\frac{\partial \boldsymbol{u}}{\partial t} \tag{3}$$

The hydrodynamics flow in porous media is governed by the combination of the continuity equation representing conservation of mass (S1) and the momentum equation (S2) based on the Navier-stokes equations as follows,

$$\frac{\partial(\varepsilon\rho)}{\partial t} + \nabla\cdot(\rho\boldsymbol{u}) = \boldsymbol{Q_m} \tag{S1}$$

$$\frac{\rho}{\varepsilon}\left(\frac{\partial \boldsymbol{u}}{\partial t} + (\boldsymbol{u}\cdot\nabla)\frac{\boldsymbol{u}}{\varepsilon}\right) = \nabla\cdot[-p\mathbf{I} + \mathbf{K}] - \left(\frac{\mu}{\kappa} + \beta\varepsilon\rho|\boldsymbol{u}| + \frac{Q_m}{\varepsilon^2}\right)\boldsymbol{u} + \mathbf{F} \tag{S2}$$

where ρ is the fluid density, ε is the porosity, $\boldsymbol{u}$ is velocity vector, p is pressure, $\mathbf{I}$ is the unit matrix, $\mathbf{K}$ is the viscous stress tensor, κ is the permeability of the porous medium, Q_m is the mass source accounting for mass deposit and mass creation within the domains, $\mathbf{F}$ is the volume force vector. Since we assume the fluid being incompressible with constant density, eq. S1 can be written as:

$$\boldsymbol{Q_m} = \mathbf{0} \tag{S3}$$

The inertial force and volume forces are ignored in our model, and there is no viscous force provided by Forchheimer and Ergun drag, thus, eq. S2 transfers into,

$$\nabla \boldsymbol{p} = -\frac{\mu}{\kappa}\boldsymbol{u} + \nabla\cdot\mathbf{K} - \frac{\rho}{\varepsilon}\frac{\partial \boldsymbol{u}}{\partial t} \tag{S4}$$

and with the condition of viscous stress tensor,

$$\mathbf{K} = \frac{\mu}{\varepsilon}\left(\nabla \boldsymbol{u} + (\boldsymbol{\nabla u})^{\mathbf{T}}\right) - \frac{2}{3}\frac{\mu}{\varepsilon}(\nabla \cdot \boldsymbol{u})\mathbf{I} = \frac{\mu}{\varepsilon}\left(\nabla \boldsymbol{u} + (\boldsymbol{\nabla u})^{\mathbf{T}}\right) \tag{S5}$$

So,

$$\nabla \cdot \mathbf{K} = \frac{\mu}{\varepsilon}\nabla \cdot \left(\nabla \boldsymbol{u} + (\boldsymbol{\nabla u})^{\mathbf{T}}\right) = \frac{\mu}{\varepsilon}\left(\nabla \cdot \nabla \boldsymbol{u} + \nabla \cdot (\boldsymbol{\nabla u})^{\mathbf{T}}\right) \tag{S6}$$

where

$$\nabla \cdot \nabla \boldsymbol{u} = \nabla \cdot \left(\frac{\partial \boldsymbol{u}}{\partial x}, \quad \frac{\partial \boldsymbol{u}}{\partial y}, \quad \frac{\partial \boldsymbol{u}}{\partial z}\right) = \left(\frac{\partial^2 \mathrm{u}}{\partial x^2}, \frac{\partial^2 \mathrm{u}}{\partial x \partial y}, \frac{\partial^2 \mathrm{u}}{\partial x \partial z}\right)^{\mathrm{T}} + \left(\frac{\partial^2 \mathrm{v}}{\partial y \partial x}, \frac{\partial^2 \mathrm{v}}{\partial y^2}, \frac{\partial^2 \mathrm{v}}{\partial y \partial z}\right)^{\mathrm{T}} + \left(\frac{\partial^2 \mathrm{w}}{\partial z \partial x}, \frac{\partial^2 \mathrm{w}}{\partial z \partial y}, \frac{\partial^2 \mathrm{w}}{\partial z^2}\right)^{\mathrm{T}}$$

$$= \begin{pmatrix} \frac{\partial}{\partial x}\left(\frac{\partial \mathrm{u}}{\partial x} + \frac{\partial \mathrm{v}}{\partial y} + \frac{\partial \mathrm{w}}{\partial z}\right) \\ \frac{\partial}{\partial y}\left(\frac{\partial \mathrm{u}}{\partial x} + \frac{\partial \mathrm{v}}{\partial y} + \frac{\partial \mathrm{w}}{\partial z}\right) \\ \frac{\partial}{\partial z}\left(\frac{\partial \mathrm{u}}{\partial x} + \frac{\partial \mathrm{v}}{\partial y} + \frac{\partial \mathrm{w}}{\partial z}\right) \end{pmatrix} = \mathbf{0} \tag{S7}$$

$$\nabla \cdot (\nabla \boldsymbol{u})^{\mathrm{T}} = \nabla \cdot \begin{pmatrix} \frac{\partial \mathrm{u}}{\partial x}, \frac{\partial \mathrm{v}}{\partial x}, \frac{\partial \mathrm{w}}{\partial x} \\ \frac{\partial \mathrm{u}}{\partial y}, \frac{\partial \mathrm{v}}{\partial y}, \frac{\partial \mathrm{w}}{\partial y} \\ \frac{\partial \mathrm{u}}{\partial z}, \frac{\partial \mathrm{v}}{\partial z}, \frac{\partial \mathrm{w}}{\partial z} \end{pmatrix} = \begin{pmatrix} \frac{\partial^2 \mathrm{u}}{\partial x^2} + \frac{\partial^2 \mathrm{u}}{\partial y^2} + \frac{\partial^2 \mathrm{u}}{\partial z^2} \\ \frac{\partial^2 \mathrm{v}}{\partial x^2} + \frac{\partial^2 \mathrm{v}}{\partial y^2} + \frac{\partial^2 \mathrm{v}}{\partial z^2} \\ \frac{\partial^2 \mathrm{w}}{\partial x^2} + \frac{\partial^2 \mathrm{w}}{\partial y^2} + \frac{\partial^2 \mathrm{w}}{\partial z^2} \end{pmatrix} = \left(\frac{\partial^2}{\partial x^2} + \frac{\partial^2}{\partial y^2} + \frac{\partial^2}{\partial z^2}\right)\begin{pmatrix} \mathrm{u} \\ \mathrm{v} \\ \mathrm{w} \end{pmatrix} = \nabla^2 \boldsymbol{u} \tag{S8}$$

Inserting eq. S7 and eq. S8 into eq. S6 gives,

$$\nabla \cdot \mathbf{K} = \frac{\mu}{\varepsilon}\nabla \cdot \left(\nabla \boldsymbol{u} + (\boldsymbol{\nabla u})^{\mathbf{T}}\right) = \frac{\mu}{\varepsilon}\left(\nabla \cdot \nabla \boldsymbol{u} + \nabla \cdot (\boldsymbol{\nabla u})^{\mathbf{T}}\right) = \frac{\mu}{\varepsilon}\nabla^2 \boldsymbol{u} \tag{S9}$$

And finally taking eq. S9 into eq. S4 results in,

$$\nabla \boldsymbol{p} = -\frac{\mu}{\kappa}\boldsymbol{u} + \frac{\mu}{\varepsilon}\nabla^2 \boldsymbol{u} - \frac{\rho}{\varepsilon}\frac{\partial \boldsymbol{u}}{\partial t} \tag{S10}$$

which equals eq. 3 in the main text. If the flow is at a stationary status, $\frac{\partial \boldsymbol{u}}{\partial t} = 0$, then eq. S10 results in the traditional Brinkman equation:

$$\nabla \boldsymbol{p} = -\frac{\mu}{\kappa}\mathbf{u} + \frac{\mu}{\varepsilon}\nabla^2 \mathbf{u} \tag{S11}$$